

Cite this: *Nanoscale*, 2017, 9, 15766

Received 9th July 2017,

Accepted 16th September 2017

DOI: 10.1039/c7nr06152h

rsc.li/nanoscale

# Large-scale metal nanoelectrode arrays based on printed nanowire lithography for nanowire complementary inverters†

Han-Seung Ko,<sup>‡a,b</sup> Yeongjun Lee,<sup>id</sup> <sup>‡a,c</sup> Sung-Yong Min,<sup>id</sup> <sup>a</sup> Sung-Joo Kwon<sup>a</sup> and Tae-Woo Lee<sup>id</sup> <sup>\*c,d,e</sup>

**Nanowire (NW) complementary inverters based on NW channels and NW electrodes are a promising core logic unit of future sub-miniature, high density and textile-type configured electronic circuits. However, existing approaches based on short NWs (<150 μm) or non-woven nanofibers cannot provide precisely-coordinated NW inverters due to the difficulty in the position and alignment control of each NW. In particular, the large-scale fabrication of highly-aligned metal nanoelectrode (NE) arrays with low resistivity is a challenging issue. Here, we developed large-scale-aligned AgNE arrays with very low resistivity by using printed NW lithography, and then demonstrated NW complementary inverters by combining with direct-printed organic semiconducting NWs. The width of the AgNEs was controlled from 250 to 1000 nm; their resistivity was 2.6 μΩ cm which is quite comparable with that of Ag films (1.6 μΩ cm). We expect that this approach will facilitate advances in the large-scale fabrication of nanoelectronics which will be compatible with printed electronics.**

Nanowire (NW) transistors and inverters composed of individually-defined semiconducting NW channels and metallic NW electrodes are expected to become key building blocks for high-density nanoelectronics.<sup>1–4</sup> Until now, research on transistors and inverters based on NWs had mainly focused on the development of semiconducting NW-based devices with metal film electrodes.<sup>5–11</sup> To realize large-scale-integrated NW transistors and inverters, uniformly-patterned and highly-conduc-

tive metal NW electrodes must be fabricated on a large area. Conventional short metal NWs (<150 μm) usually produced randomly-distributed two-dimensional (2D) conductive mats that have percolation networks with a lot of junctions between the NWs.<sup>12–17</sup> Such conductive films suffered from rough surface morphology, low dispersion uniformity, and uncontrollable alignment and positioning of individual NWs.

Electrospinning is another method to construct very long and continuous metal NW networks by using an easy and cost-effective solution process. However, electrospun metal NWs converted from polymer/metal precursor composite NWs require high temperature annealing (>300 °C) which limits the selection of substrates and materials. Moreover, these polycrystalline metal NWs have relatively higher resistivity (>13 times) than those of bulk metals.<sup>18–20</sup> On the other hand, a combination of metal evaporation and the electrospun organic NW networks produces highly-conductive metal NW networks by patterning metal thin layers using randomly-coiled long and continuous NWs as masks.<sup>21–23</sup> However, all previous electrospinning-based methods produce only non-woven or roughly-aligned metal NW networks so that they cannot develop large-scale-integrated NW transistors and inverters with NW channels and NW electrodes. Therefore, a process that does not have these limitations should be developed.

In this work, we reported printed NW lithography (PNL) to fabricate a simply-patterned and position- and dimension-controllable 1D Ag nanoelectrode (AgNE) array with low resistivity by using electrohydrodynamic NW printing (E-NP) which is a simple, inexpensive and rapid process to control the large-scale-aligned NW arrays. Our precisely-arranged AgNE was nearly as conductive (resistivity ~2.6 μΩ cm) as bulk Ag (1.6 μΩ cm), whose resistivity was much lower than those of previously reported electrospun polycrystalline AgNWs obtained from thermal treatment (5.7–20.8 μΩ cm).<sup>4,20</sup> Compared to the previously-reported metal NW networks produced by patterning methods using randomly-oriented inorganic short NWs (<10 μm) grown by chemical synthesis or using randomly-coiled non-woven electrospun NW networks as patterning masks,<sup>21–25</sup> our direct-printed, highly-aligned, arbitrarily-long and pattern-customizable

<sup>a</sup>Department of Materials Science and Engineering, Pohang University of Science and Technology (POSTECH), Pohang 37673, Republic of Korea

<sup>b</sup>Department of Chemical and Biological Engineering, Seoul National University, Seoul 08826, Republic of Korea

<sup>c</sup>Department of Materials Science and Engineering, Seoul National University, Seoul 08826, Republic of Korea

<sup>d</sup>Research Institute of Advanced Materials, Seoul National University, Seoul 08826, Republic of Korea

<sup>e</sup>BK21 PLUS SNU Materials Division for Educating Creative Global Leaders, Seoul National University, Seoul 08826, Republic of Korea. E-mail: twlees@snu.ac.kr, taewlees@gmail.com

†Electronic supplementary information (ESI) available. See DOI: 10.1039/c7nr06152h

‡These authors contributed equally to this work.

AgNE arrays were much appropriate for use as source and drain (S/D) electrodes for transistor and inverter arrays, which is promising to replace the conventional optical lithography processes for fabricating nano-sized electrode arrays on a large area. We demonstrated NW transistors and complementary inverters composed of highly-aligned organic semiconducting (OSC) NWs and AgNEs; this is the first NW inverter (voltage gain  $\sim 18$ ) fabricated by non-contact direct printing. We expect our AgNEs patterned by the PNL process to have a wide applicability owing to their easy, simple and heating-free procedures to control the width, number, spacing, location, direction and orientation,<sup>26,27</sup> and good adhesion between the metal film and substrates.

To fabricate AgNE arrays by PNL, a highly-conductive Ti (3 nm)/Ag thin layer (100 nm) was thermally evaporated onto a SiO<sub>2</sub> (100 nm)/Si substrate (Fig. 1a). A precisely-controlled chemical wet etching mask of a poly(vinylidene fluoride-co-trifluoroethylene) (PVDF-TrFE) organic NW array was printed onto the Ti/Ag thin layer. Various patterns of NWs were simply obtained by adjusting parameters such as printing speed, direction and location. Local spiraling caused by repulsion among positively-charged NWs under high electric field within a short distance (7 mm) between a nozzle tip and a grounded substrate resulted in spontaneously coiled NWs while the collector was not moving (ESI Fig. 1†). Therefore, when the moving speed of the collector is fast enough, linear NW arrays are produced (Fig. 1b and c) and when the speed is slower than the nanowire jetting speed, serpentine NW arrays are produced (Fig. 1d).

An as-printed pristine PVDF-TrFE NW has a perfectly circular cylinder shape so that it has a small contact area with the surface of the Ag layer (Fig. 2a). This small adhesion cannot prevent the etchant from soaking under the NW masks, and therefore impedes the formation of continuous and conducting NE arrays after wet etching (Fig. 2b). Therefore, a solvent vapor annealing step using tetrahydrofuran (THF) to collapse the PVDF-TrFE NW was conducted at 45 °C to increase the contact area between the NW mask and the Ag film. As the annealing time  $t_{\text{ann}}$  was increased, the NW became progressively flatter, and the contact area enlarged until the annealing time  $t_{\text{ann}} = 40$  min (width  $\sim 1.2$   $\mu\text{m}$ ) (Fig. 2c and d); no further change occurred at  $t_{\text{ann}} > 40$  min (ESI Fig. 2†). A mixture of ammonium hydroxide (NH<sub>4</sub>OH), hydrogen peroxide (H<sub>2</sub>O<sub>2</sub>) and methanol (CH<sub>3</sub>OH) was used as a chemical etchant to remove the regions of the Ti/Ag layer that were not protected by the NW masks.

The composition of the etchant mixture was important for the formation of AgNEs (ESI Fig. 3†). When the amount of CH<sub>3</sub>OH was too high (NH<sub>4</sub>OH:H<sub>2</sub>O<sub>2</sub>:CH<sub>3</sub>OH = 1:1:1 or 1:1:0.5), the boundaries of the Ag layers were not clear because a weak etchant needs sufficient time to remove the Ag layer; during this time the etchant slightly diffused under the masks irregularly and resulted in rough edges (ESI Fig. 3a and b†). The etchant without dilution (NH<sub>4</sub>OH:H<sub>2</sub>O<sub>2</sub>:CH<sub>3</sub>OH = 1:1:0) removed the Ag layer too fast, so that the pattern boundary was also unclear (ESI Fig. 3d†). In our case, an

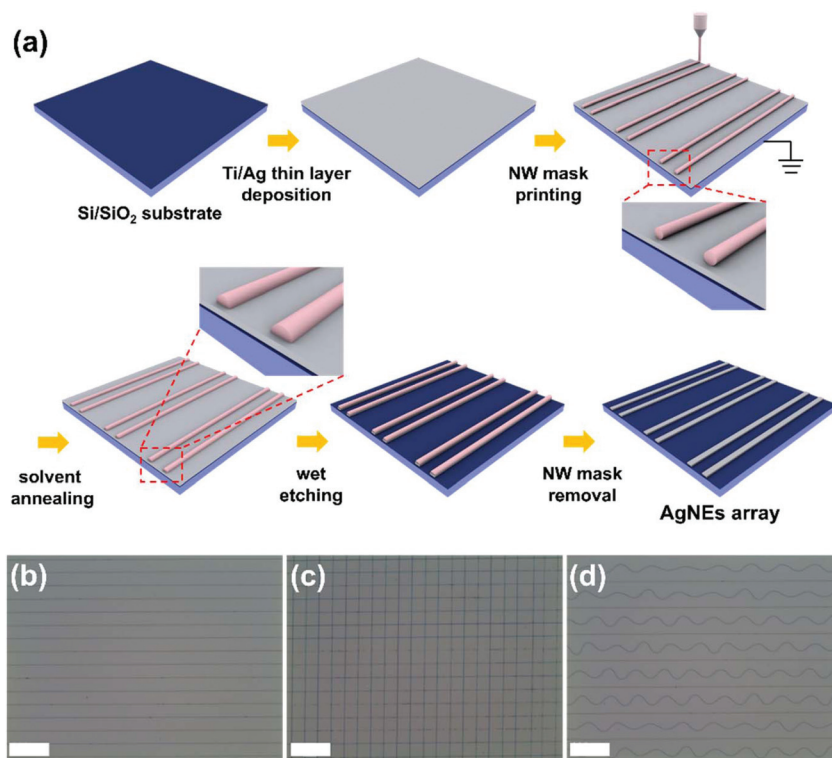


**Fig. 1** AgNE arrays fabricated by PNL. (a) Schematic description of the fabrication procedures of AgNEs by PNL. A NW mask array was printed by E-NP. Scanning electron microscopy (SEM) images of AgNE arrays with various patterns: (b) parallel lines, (c) perpendicular grid lines, and (d) alternate straight and serpentine lines (scale bar: 300  $\mu\text{m}$ ).

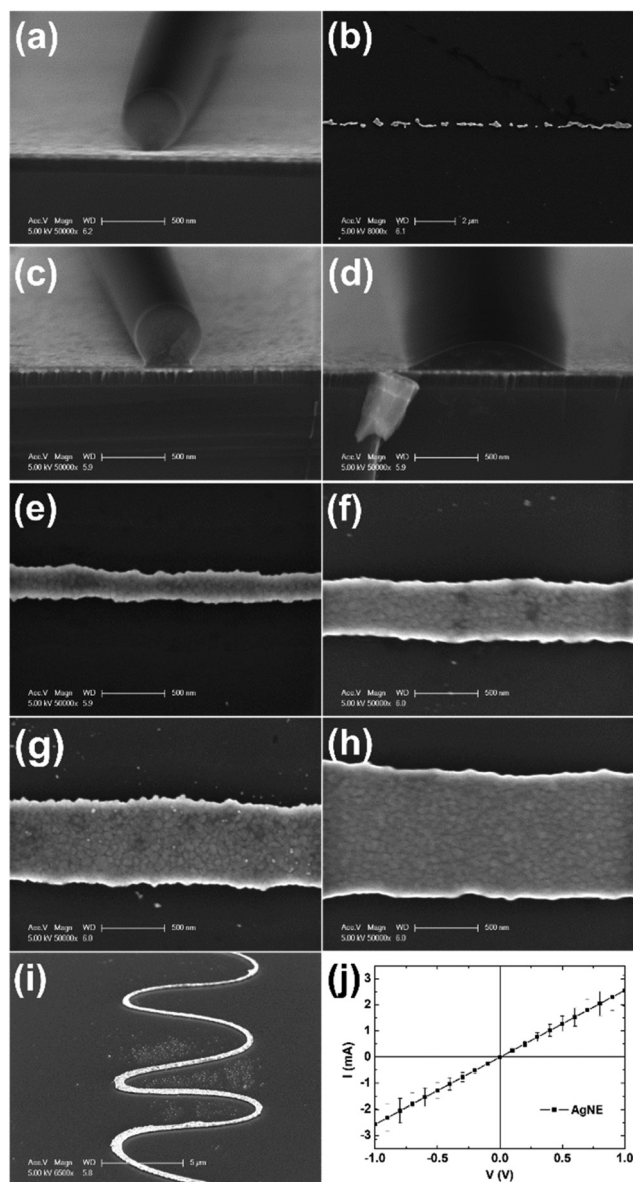
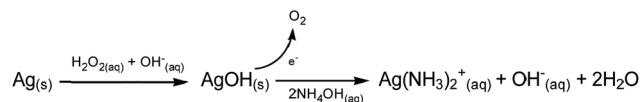


**Fig. 2** SEM images of PVDF-TrFE NW masks and resultant AgNE patterns after wet etching at different solvent vapor annealing times. (a) Cross view of PVDF-TrFE NW masks and (b) top view of resultant AgNE patterns without solvent vapor annealing. Cross-section of PVDF-TrFE NW masks with solvent vapor annealing for (c) 20 and (d) 40 min. Top morphology of AgNEs with widths of (e) 250, (f) 500, (g) 750, and (h) 1000 nm. (i) Serpentine pattern of the AgNE. (j)  $I$ - $V$  curve of each single AgNE. The average resistivity is  $2.6 \pm 0.3 \mu\Omega \text{ cm}$ .

etchant mixture ratio of  $\text{NH}_4\text{OH}:\text{H}_2\text{O}_2:\text{CH}_3\text{OH} = 1:1:0.25$  was quite appropriate to obtain clear pattern edges (ESI Fig. 3c†).

The specific etching mechanism while the sample was immersed in the etchant mixture is as follows:<sup>28,29</sup> first,  $\text{H}_2\text{O}_2$  oxidized Ag to AgOH, which then reacted with  $\text{NH}_4\text{OH}$  to form  $\text{Ag}(\text{NH}_3)_2^+$  which is soluble in the etchant. A thin Ti layer (3 nm) was also etched away by the etching solution (Scheme 1).



**Scheme 1** Etching mechanism of the Ag layer.

The etchant was washed away using copious flow of water. These procedures did not affect the PVDF-TrFE NWs. Finally, the NW masks were removed by washing with acetone. The result was a uniformly-patterned, highly-conductive and large-scale AgNE array.

With various bottom areas of the collapsed NW masks, the width of the AgNEs was controlled from 250 to 1000 nm (Fig. 2e-h). A serpentine AgNE was also developed (Fig. 2i); it might be potentially used in flexible and stretchable devices in the near future.

The current-voltage ( $I$ - $V$ ) curve of the AgNWs showed an average resistivity of  $2.6 \pm 0.3 \mu\Omega \text{ cm}$  which is only 1.6 times higher than that of bulk Ag ( $1.6 \mu\Omega \text{ cm}$ ) (Fig. 2j). The resistivity of the AgNEs was consistent regardless of the pattern width and was excellent compared to that of the previously reported AgNWs which had a higher resistivity due to organic residues and many grain boundaries in the polycrystalline nanofiber.<sup>4,20</sup>

NW complementary inverters were realized with two p- and n-type NW field-effect transistors (FETs) composed of p- or n-type OSC NWs as active channels and AgNEs as S/D electrodes (Fig. 3). OSC NWs in the NW devices were also fabricated by E-NP (Fig. 3a). For the comparison of the intrinsic electrical properties of p- and n-type OSC NW FETs, 10 strands of p- and n-type OSC NWs were printed on the S/D electrodes. In the NW inverters, the output currents of each NW FET were easily balanced by adjusting the number of OSC NWs.

Before the wet etching step, the PVDF-TrFE solution was drop-cast to form Ag contact pads for measuring probes (ESI Fig. 4†). On the pre-patterned AgNE array, two kinds of OSC NWs were printed;<sup>27</sup> one was an n-type poly[ $N,N'$ -bis(2-octyldodecyl)-naphthalene-1,4,5,8-bis(dicarboximide)-2,6-diyl]-*alt*-5,5',9,9'-bithiophene} (P(NDI2OD-T2), Polyera ActivInk N2200) OSC NW and the other was a p-type poly(3-hexylthiophene-2,5-diyl) (P3HT) OSC NW (Fig. 3b). The OSC NWs were thermally annealed at 150 °C over 30 min under vacuum to improve the contact between the OSC NWs and the electrodes. In this step, bottom-gate and bottom-contact (BG-BC) geometric NW FETs and an inverter were constructed (ESI Fig. 5a†). Highly-doped Si and a  $\text{SiO}_2$  (100 nm) layer under the AgNEs were used as the gate electrode and dielectric layer of BG-BC geometric NW devices. To develop high electrical performance inverters, the FETs must have high output currents. Therefore, we cast a PVDF-TrFE high- $k$  polymer dielectric layer (500 nm) on the OSC NWs for the fabrication of a top-gate and bottom-contact (TG-BC) configuration based on the higher dielectric constant (10.4) of PVDF-TrFE than that (3.9) of  $\text{SiO}_2$  (Fig. 4a).<sup>30,31</sup> Al gate electrodes (100 nm) were thermally-deposited on the polymer dielectric layer using metal shadow masks (Fig. 3a).



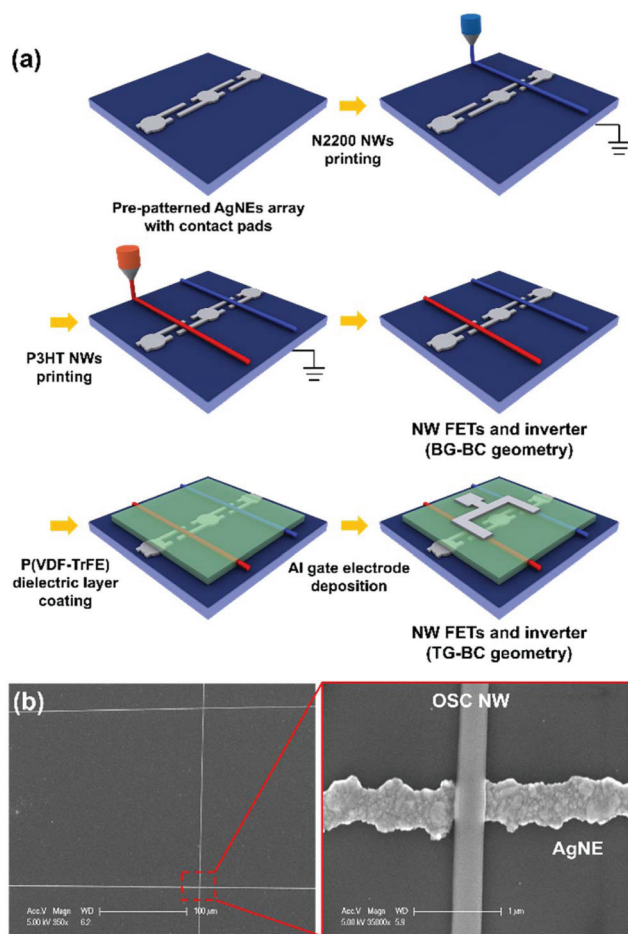


**Fig. 3** NW FETs and inverters with AgNEs. (a) Schematic description of the fabrication procedures of NW FETs and inverters. (b) SEM images of cross junction of OSC NWs and AgNEs.

Regardless of the device configuration (*i.e.* BG-BC and TG-BC) of FETs (ESI Fig. 5a and 4a†), p-type NW FETs had a higher field-effect hole mobility ( $\mu_{h,BG-BC,AgNE} \sim 1.04 \times 10^{-3} \text{ cm}^2 \text{ V}^{-1} \text{ s}^{-1}$ ,  $\mu_{h,TG-BC,AgNE} \sim 6.70 \times 10^{-1} \text{ cm}^2 \text{ V}^{-1} \text{ s}^{-1}$ ) than p-type control FETs composed of P3HT NWs and Ag thin film S/D electrodes ( $\mu_{h,BG-BC,Ag \text{ film}} \sim 5.20 \times 10^{-4} \text{ cm}^2 \text{ V}^{-1} \text{ s}^{-1}$ ,  $\mu_{h,TG-BC,Ag \text{ film}} \sim 4.52 \times 10^{-1} \text{ cm}^2 \text{ V}^{-1} \text{ s}^{-1}$ ) (ESI Fig. 5b and 4b†). In contrast, n-type control devices with N2200 NWs had a slightly higher field-effect electron mobility ( $\mu_{e,BG-BC,Ag \text{ film}} \sim 1.44 \times 10^{-2} \text{ cm}^2 \text{ V}^{-1} \text{ s}^{-1}$ ,  $\mu_{e,TG-BC,Ag \text{ film}} \sim 8.15 \times 10^{-2} \text{ cm}^2 \text{ V}^{-1} \text{ s}^{-1}$ ) than n-type NW FETs ( $\mu_{e,BG-BC,AgNE} \sim 1.14 \times 10^{-2} \text{ cm}^2 \text{ V}^{-1} \text{ s}^{-1}$ ,  $\mu_{e,TG-BC,AgNE} \sim 4.42 \times 10^{-2} \text{ cm}^2 \text{ V}^{-1} \text{ s}^{-1}$ ) (ESI Fig. 5c and 4c†). These mobility variations resulted from the difference in the carrier injection barrier between the work function WF of the electrode and the highest occupied molecular orbital (HOMO) of the P3HT p-type semiconductor or the lowest unoccupied molecular orbital (LUMO) of the N2200 n-type semiconductor.

The WFs of both the AgNE and Ag film were analyzed by Kelvin Probe measurement. In comparison with the WF of the Ag film, the AgNE had 0.2 eV higher WF because of the surface oxidation of the AgNE during wet etching (ESI Fig. 6†).

Because the HOMO (5.0 eV) of P3HT is better-matched with the WF of the AgNE than the WF of the Ag film, the higher  $\mu_{h,AgNE}$  of p-type NW FETs than the  $\mu_{h,Ag \text{ film}}$  of p-type control FETs is reasonable. However, in n-type N2200 NW devices, the WF of the Ag film is more comparable with the LUMO (4.0 eV) of N2200 than the WF of the AgNE. Therefore, n-type control devices with Ag film electrodes showed a slightly higher electron mobility than n-type NW FETs.

Despite the increased WF of the AgNEs, the intrinsic carrier mobility of n-type N2200 NWs was 10 times higher than that of p-type P3HT NWs in the BG-BC NW FETs, so BG-BC NW complementary inverters were fabricated with 10 times more P3HT NWs (100 strands) than N2200 NWs (10 strands) to match the output currents of both devices (ESI Fig. 5d†). Because of the well-balanced characteristics of p- and n-type FETs, the voltage transfer characteristic (VTC) was stable and the switching threshold voltage  $V_M$  was 15.2 V, which is very close to half of the supply voltage  $V_{DD}$ , and the voltage gain was 6 (ESI Fig. 5e†).

TG-BC geometric p-type NW FETs with a high- $k$  polymer PVDF-TrFE dielectric layer had a hole mobility  $\mu_{h,TG-BC,AgNE} \sim 6.70 \times 10^{-1} \text{ cm}^2 \text{ V}^{-1} \text{ s}^{-1}$  that was more than two orders of magnitude higher than that of p-type NW FETs with the BG-BC configuration ( $\mu_{h,BG-BC,AgNE} \sim 1.04 \times 10^{-3} \text{ cm}^2 \text{ V}^{-1} \text{ s}^{-1}$ ) because PVDF-TrFE has many fluorine moieties which have strong electronegativity, so they cause better hole accumulation at the interface between the PVDF-TrFE dielectric layer and the P3HT NW than at the interface between the  $\text{SiO}_2$  dielectric layer and the P3HT NW.<sup>30,31</sup> In n-type NW FETs, a small enhancement was obtained in TG-BC geometric devices ( $\mu_{e,TG-BC,AgNE} \sim 4.42 \times 10^{-2} \text{ cm}^2 \text{ V}^{-1} \text{ s}^{-1}$ ) compared to the BG-BC structure ( $\mu_{e,BG-BC,AgNE} \sim 1.14 \times 10^{-2} \text{ cm}^2 \text{ V}^{-1} \text{ s}^{-1}$ ) because the fluorine moieties of PVDF-TrFE were not effective for the accumulation of electrons at the interface between the polymer dielectric layer and the n-type semiconducting N2200 NW.<sup>30,31</sup>

In contrast to BG-BC geometric FETs, the TG-BC p-type NW FETs showed almost 10 times higher carrier mobility than the n-type NW FETs. Therefore, 10 times more N2200 NWs (100 strands) were printed than P3HT NWs (10 strands) in the TG-BC NW complementary inverters (Fig. 4d); as a result of the much increased output current of FETs we achieved an excellent switching behavior with  $V_M = 27.2 \text{ V}$  and a voltage gain of 18 (Fig. 4e).

In conclusion, we developed large-scale NW complementary inverters based on novel position- and dimension-controllable 1D AgNE arrays with low resistivity that were fabricated by a very simple PNL patterning process. The width of the AgNEs was controlled from 250 to 1000 nm and their average resistivity was  $2.6 \mu\Omega \text{ cm}$ , which is only 1.6 times higher than that of bulk Ag. This first NW inverter array realized by a non-contact direct-printing method showed a voltage gain of 18. Based on these results, we expect that more complicated logic gates such as NAND and NOR gates can also be developed with metal NEs. Our process does not use any complicated, expensive electron beam and optical lithography. Therefore, our approach would be promising to generate potential alternative nanoelectrodes for future applications of printed nanoelectronics by replacing

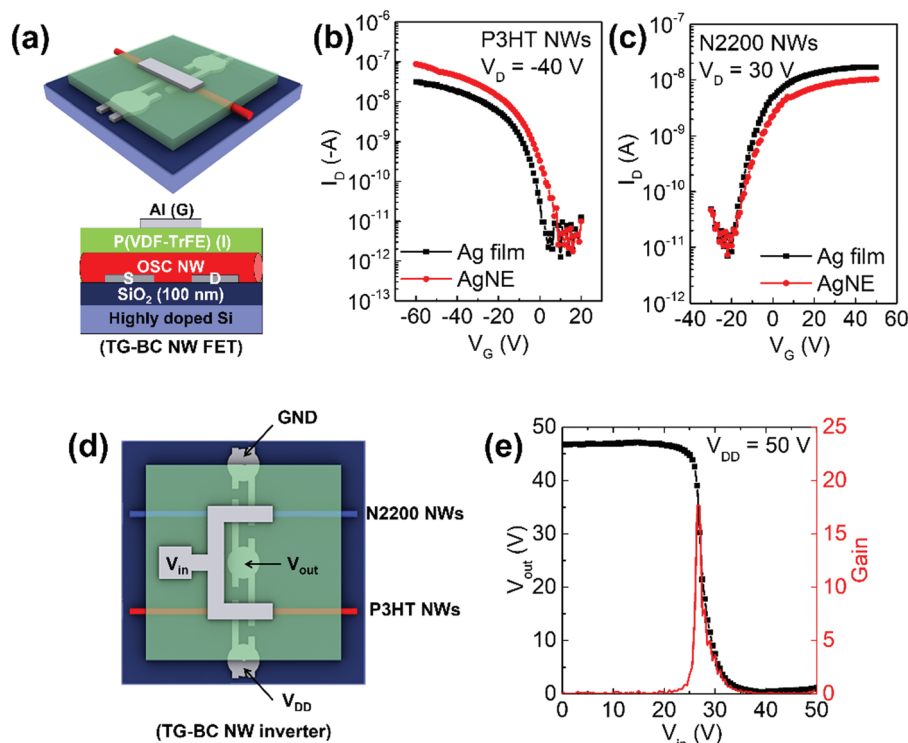


**Fig. 4** Characteristics of TG-BC geometric NW FETs and inverters with a PVDF-TrFE dielectric layer. (a) Specific device structure of NW FETs. Transfer characteristics of NW FETs with (b) p-type P3HT and (c) n-type N2200 NWs compared to control devices with Ag film electrodes. Each FET was composed of 10 strands of OSC NWs. (d) Specific device structure of the NW inverter. (e) VTC and voltage gain characteristic of NW complementary inverters composed of 10 strands of P3HT NWs, 100 strands of N2200 NWs, and AgNEs.

the conventional electron-beam and optical lithography processes to make nanoscale-patterned metal thin film electrodes.

## Experimental section

### Organic nanowire wet etching mask preparation

Poly(vinylidene fluoride-co-trifluoroethylene) (PVDF-TrFE, 75:25, Solvay) was dissolved (15 wt%) in a solvent mixture of *N,N*-dimethylformamide (DMF, Aldrich) and tetrahydrofuran (THF, Aldrich) (*w:w* = 1:4). The solution was mixed using a magnetic stirring bar for 3 h to make a transparent homogeneous polymer solution. The solution was loaded into a glass syringe (1 mL, Hamilton) which was connected to a metallic nozzle tip (inner diameter = 100  $\mu\text{m}$ ). The solution flow rate was 0.17  $\mu\text{L min}^{-1}$ , and a voltage of 1.1 kV was applied to the syringe. The tip-to-collector distance was 7 mm and the stage moving speed was 1000  $\text{mm s}^{-1}$  (electrohydrodynamic organic NW printer, Enjet Inc.).

The as-printed pristine PVDF-TrFE nanowires were annealed at 45  $^{\circ}\text{C}$  with THF vapor to transform the perfectly-circular cross-section of the PVDF-TrFE nanowire into a semi-circular shape.

### Ag wet etching

$\text{NH}_4\text{OH}$  (ammonium hydroxide solution, 28–30% in  $\text{H}_2\text{O}$ , Aldrich),  $\text{H}_2\text{O}_2$  (hydrogen peroxide, 30% in  $\text{H}_2\text{O}$ , Daejung) and

$\text{CH}_3\text{OH}$  (methanol, Samchun) were mixed in various volume ratios. The substrate with organic nanowire masks on the thermally evaporated Ti (3 nm)/Ag film (100 nm) was immersed in a chemical etchant solution for  $\sim 1$  s and then rinsed using distilled water (Samchun) and acetone (Samchun) sequentially to remove the residual etchant and organic nanowire masks, and then blown dry using an  $\text{N}_2$  gun.

### Fabrication of NW FETs and inverters

Poly(3-hexylthiophene-2,5-diyl) (P3HT, Aldrich) and poly(ethylene oxide) (PEO,  $M_w$  = 400 000, Aldrich) were mixed (*w:w* = 7:3) in a solvent mixture of chlorobenzene (CB, Aldrich) and trichloroethylene (TCE, Aldrich) (*w:w* = 2:1.3). The concentration of P3HT:PEO in the solution was 3.37 wt%. The solution was stirred at 50  $^{\circ}\text{C}$  for 30 min, then loaded into a glass syringe (1 mL, Hamilton) that was connected to a metallic nozzle tip (inner diameter = 100  $\mu\text{m}$ , Enjet Inc.). The solution flow rate was 0.17  $\mu\text{L min}^{-1}$ , and a voltage of 1.1 kV was applied to the syringe. The tip-to-collector distance was 5.5 mm and the stage moving speed was 750  $\text{mm s}^{-1}$ . The printed P3HT nanowires were annealed at 150  $^{\circ}\text{C}$  for 30 min under vacuum. The diameter of the P3HT nanowire was 330 nm.

Poly{[*N,N*9-bis(2-octyldodecyl)-naphthalene-1,4,5,8-bis(dicarboximide)-2,6-diyl]-alt-5,9-(2,29-bithiophene)} (N2200 (Polyera ActivInk), P(NDI2OD-T2)) and PEO ( $M_w$  = 400 000, Aldrich)

were mixed (w:w = 7:3) in a solvent mixture of CB and TCE (w:w = 2:1.3). The concentration of N2200:PEO in the solution was 3.53 wt%. The solution was stirred at 50 °C for 60 min, and then loaded into a glass syringe (500 µL, Hamilton) which was connected to a metallic nozzle tip (inner diameter = 100 µm, Enjet Inc.). The solution flow rate was 0.12 µL min<sup>-1</sup>; and a voltage of 1.1 kV was applied to the syringe. The tip-to-collector distance was 5.5 mm and the stage moving speed was 900 mm s<sup>-1</sup>. The printed N2200 nanowires were annealed at 150 °C for 1 h under vacuum. The diameter of the N2200 nanowire was 310 nm.

For the BG-BC structure with a channel length of 50 µm, P3HT or N2200 nanowires were printed on the AgNEs. The substrate was Si/SiO<sub>2</sub> (100 nm). The AgNEs were disconnected using a probe measuring tip to act as S/D electrodes.

For the TG-BC structure with a channel length of 50 µm, on the BG-BC structure, a PVDF-TrFE solution in 2-butanone (40 mg mL<sup>-1</sup>) was spin-coated at 4000 rpm for 90 s, and then annealed at 80 °C for 2 h under N<sub>2</sub> to form a 500 nm-thick dielectric layer. The Al for the gate electrode (100 nm) was thermally evaporated onto the dielectric layer through a metal shadow mask.

### Characterization

The morphology of the AgNEs was obtained by using an optical microscope (Olympus) and a scanning electron microscope (Philips Electron Optics B.V.). The work functions of the AgNEs and the Ag film were analyzed using a Kelvin Probe (KP Technology). The electrical characteristics of FETs and inverters were evaluated using semiconductor parameter analyzers (Keithley 4200 and Keysight B1500).

## Conflicts of interest

There are no conflicts to declare.

## Acknowledgements

This work was supported by the Center for Advanced Soft-Electronics funded by the Ministry of Science, ICT and Future Planning as Global Frontier Project (2013M3A6A5073175), and the Nano Material Technology Development Program through the National Research Foundation of Korea (NRF) funded by the Ministry of Science, ICT & Future Planning (MSIP, Korea) (NRF-2014M3A7B4051747).

## Notes and references

- K. S. Park, B. Cho, J. Baek, J. K. Hwang, H. Lee and M. M. Sung, *Adv. Funct. Mater.*, 2013, **23**, 4776–4784.
- Q. Tang, Y. Tong, W. Hu, Q. Wan and T. Bjørnholm, *Adv. Mater.*, 2009, **21**, 4234–4237.
- S.-Y. Min, Y. Lee, S. H. Kim, C. Park and T.-W. Lee, *ACS Nano*, 2017, **11**, 3681–3689.
- Y. Lee, S.-Y. Min, T.-S. Kim, S.-H. Jeong, J. Y. Won, H. Kim, W. Xu, J. K. Jeong and T.-W. Lee, *Adv. Mater.*, 2016, **28**, 9109–9116.
- A. L. Briseno, S. C. B. Mannsfeld, S. A. Jenekhe, Z. Bao and Y. Xia, *Mater. Today*, 2008, **11**, 38–47.
- J. H. Oh, H. W. Lee, S. Mannsfeld, R. M. Stoltenberg, E. Jung, Y. W. Jin, J. M. Kim, J.-B. Yoo and Z. Bao, *Proc. Natl. Acad. Sci. U. S. A.*, 2009, **106**, 6065–6070.
- J. Wu, Q. Li, G. Xue, H. Chen and H. Li, *Adv. Mater.*, 2017, **29**, 1606101.
- G. Xue, J. Wu, C. Fan, S. Liu, Z. Huang, Y. Liu, B. Shan, H. L. Xin, Q. Miao, H. Chen and H. Li, *Mater. Horiz.*, 2016, **3**, 119–123.
- S. Lee, G. D. Moon and U. Jeong, *J. Mater. Chem.*, 2009, **19**, 743–748.
- S. W. Lee, H. J. Lee, J. H. Choi, W. G. Koh, J. M. Myoung, J. H. Hur, J. J. Park, J. H. Cho and U. Jeong, *Nano Lett.*, 2010, **10**, 347–351.
- S.-Y. Min, T.-S. Kim, Y. Lee, H. Cho, W. Xu and T.-W. Lee, *Small*, 2015, **11**, 45–62.
- J.-H. Chang, K.-M. Chiang, H.-W. Kang, W.-J. Chi, J.-H. Chang, C.-I. Wu and H.-W. Lin, *Nanoscale*, 2015, **7**, 4572–4579.
- Y.-J. Shiao, K.-M. Chiang and H.-W. Lin, *Nanoscale*, 2015, **7**, 12698–12705.
- T. Akter and W. S. Kim, *ACS Appl. Mater. Interfaces*, 2012, **4**, 1855–1859.
- J. S. Park, M. Rezaei and W. S. Kim, *Adv. Eng. Mater.*, 2014, **16**, 905–908.
- D. O. Shin, J. H. Mun, G.-T. Hwang, J. M. Yoon, J. Y. Kim, J. M. Yun, Y. Yang, Y. Oh, J. Y. Lee, J. Shin, K. J. Lee, S. Park, J. U. Kim and S. O. Kim, *ACS Nano*, 2013, **7**, 8899–8907.
- J. Y. Kim, B. H. Kim, J. O. Hwang, S.-J. Jeong, D. O. Shin, J. H. Mun, Y. J. Choi, H. M. Jin and S. O. Kim, *Adv. Mater.*, 2013, **25**, 1331–1335.
- M. Park, J. Im, M. Shin, Y. Min, J. Park, H. Cho, S. Park, M.-B. Shim, S. Jeon, D.-Y. Chung, J. Bae, J. Park, U. Jeong and K. Kim, *Nat. Nanotechnol.*, 2012, **7**, 803–809.
- M. Bognitzki, M. Becker, M. Graeser, W. Massa, J. H. Wendorff, A. Schaper, D. Weber, A. Beyer, A. Götzhäuser and A. Greiner, *Adv. Mater.*, 2006, **18**, 2384–2386.
- H. Wu, D. Lin, R. Zhang and W. Pan, *Chem. Mater.*, 2007, **19**, 1895–1897.
- T. He, A. Xie, D. H. Reneker and Y. Zhu, *ACS Nano*, 2014, **8**, 4782–4789.
- C. Bao, J. Yang, H. Gao, F. Li, Y. Yao, B. Yang, G. Fu, X. Zhou, T. Yu, Y. Qin, J. Liu and Z. Zou, *ACS Nano*, 2015, **9**, 2502–2509.
- H. Wu, D. Kong, Z. Ruan, P. Hsu, S. Wang, Z. Yu, T. J. Carney, L. Hu, S. Fan and Y. Cui, *Nat. Nanotechnol.*, 2013, **8**, 421–425.
- A. Colli, A. Fasoli, S. Pisana, Y. Fu, P. Beecher, W. I. Milne and A. C. Ferrari, *Nano Lett.*, 2008, **8**, 1358–1362.

- 25 L. Liao, Y.-C. Lin, M. Bao, R. Cheng, J. Bai, Y. Liu, Y. Qu, K. L. Wang, Y. Huang and X. Duan, *Nature*, 2010, **467**, 305–308.
- 26 Y. Lee, S.-Y. Min and T.-W. Lee, *Macromol. Mater. Eng.*, 2017, 1600507.
- 27 S.-Y. Min, T.-S. Kim, B. J. Kim, H. Cho, Y.-Y. Noh, H. Yang, J. H. Cho and T.-W. Lee, *Nat. Commun.*, 2013, **4**, 1773.
- 28 Y. Xia, E. Kim and G. M. Whitesides, *J. Electrochem. Soc.*, 1996, **143**, 1070–1079.
- 29 J. E. A. M. van den Meerakker, J. P. Metsemakers and J. B. Giesbers, *J. Electrochem. Soc.*, 2002, **149**, C256–C260.
- 30 K.-J. Baeg, D. Khim, J. Kim, H. Han, S.-W. Jung, T.-W. Kim, M. Kang, A. Facchetti, S.-K. Hong, D.-Y. Kim and Y.-Y. Noh, *ACS Appl. Mater. Interfaces*, 2012, **4**, 6176–6184.
- 31 D. Khim, Y. Xu, K.-J. Baeg, M. Kang, W.-T. Park, S.-H. Lee, I.-B. Kim, J. Kim, D.-Y. Kim, C. Liu and Y.-Y. Noh, *Adv. Mater.*, 2016, **28**, 518–526.